Tellus (2004), 56A, 536–547
Printed in UK. All rights reserved

TELLUS

Resonant inertial oscillations in moored buoy ocean surface winds

By R. G. STOCKWELL[1]*, W. G. LARGE[2] and R. F. MILLIFF[1], [1]*Colorado Research Associates Division, Northwest Research Associates Inc., 3380 Mitchell Lane, Boulder, CO 80301, USA;* [2]*Climate and Global Dynamics Division NCAR, PO Box 3000, Boulder, CO 80307-3000, USA*

(Manuscript received 26 February 2004; in final form 2 June 2004)

ABSTRACT

The surface winds from the moored buoy data set available from the National Data Buoy Center are examined for the occurrence of inertial range oscillations in the surface winds by employing a novel joint time frequency analysis of the two-component vector winds. This data set was chosen for its high time resolution (1-h sampling) that enabled the full characterization of these inertial oscillations, its at least partially global coverage, and its record length, which is needed to extract the signals from the background noise. The observation system is comprised of over 200 sites with measurements as far back as 1972.

Because of the large amount of data, many harmonics of the diurnal atmospheric tidal signature in the surface winds (24, 12, 8, and 3 h) were found in high-precision power spectra. These tidal oscillations are found to be important contributors to the inertial range oscillation at latitudes of 30°, where the largest inertial range oscillations are found. By turning to local (in time) spectral analysis using the S-transform, considerable energy was also found in the inertial frequency ranges at other latitudes, typically in the form of very large (>10 m s^{-1}), yet short-lived (of the order of a few days) events. The surface wind rotation direction in near inertial frequency bands favors resonant inertial oscillations at all latitudes, and in every season of the year.

1. Introduction

A ubiquitous feature of upper ocean currents are oscillations near the local inertial frequency with an anticyclonic (i.e. clockwise in the Northern Hemisphere) sense of rotation (Webster, 1968). There is strong evidence from both observations (Anderson et al., 1983) and modeling efforts (Fu, 1981; Poulain, 1990; Kudryavtsev, 1994; Pereira and Mascarenhas, 1994; Levine and Zervakis, 1995) that these oscillations in the ocean can be forced by the surface wind field. In particular, inertial oscillations can be generated by the sudden onset of a steady wind blowing over an ocean mixed layer (Pollard and Millard, 1970) and play a major role in deepening the layer (Pollard et al., 1973). Deeper inertial motions are developed at the expense of the mixed layer by vertical energy propagation (D'Asaro 1995), as indicated by upward propagating phase fronts (Pollard, 1980; Halle and Pinkel, 2003; Firing et al., 1997; Qi et al., 1995).

Inertial variability in surface winds is much less dominant, but has been observed at various sites (Burt et al., 1974; Mori, 1990). Therefore, there is the potential for such winds to resonate with the upper ocean currents that they generate (Pollard and Millard, 1970; Crawford and Large, 1996). Inertially rotating surface wind forcing in concert with the inertial currents has been observed to produce dramatic resonant responses in the upper ocean, especially in sea surface temperature (Large and Crawford, 1995).

However, the distribution in time and space, and the strength of inertially varying winds is not well known. In order to address this question, the surface winds from the National Data Buoy Center (NDBC) moored buoy data set (Section 2) are examined for variability at near inertial frequencies. In Section 3 we review concepts pertinent to the analyses of rotating vector time series. In Section 4, a variety of standard power spectral methods are employed to detect signals such as the atmospheric tides (inertial at specific latitudes) that are always present and maintain coherent phase. In Section 5, we introduce a novel application of time-local spectral analysis tools to characterize inertial wind events that, because of their transient nature, arrive at a mooring location with incoherent phase. A summary is provided in the final section of the paper. An appendix provides the formal mathematical definition of the time-local spectral analysis method, i.e. the S-transform, that is used in Section 5.

---

*Corresponding author.
e-mail: stockwell@co-ra.com

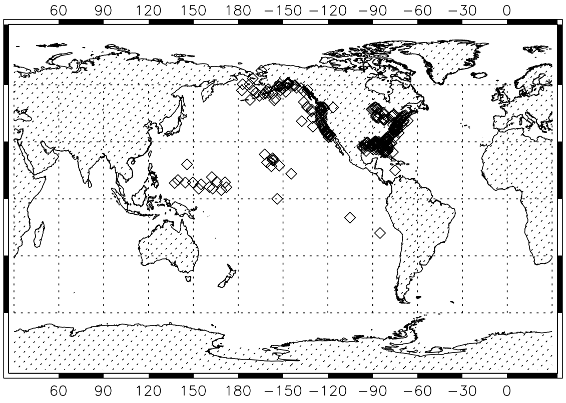

Fig 1. Location (diamond) of the 262 moored buoys from the NDBC historical STDMET data set (http://seaboard.ndbc.noaa.gov/).

2. Data

The NDBC records consist of meteorological data from the distribution of moored buoys depicted in Fig. 1. Time series for many of the buoys span several decades, with long periods at hourly resolution. The number of stations reporting per year for each region is shown in Fig. 2. For the purposes of this paper, we require very long data sets with frequent sampling in order to extract what may be very small signals in the midst of energetic background noise.

The data are checked to eliminate gross errors. Transmission parity error, range limit, and time continuity checks are performed. Measurements from duplicate sensors are compared to ensure that they are consistent. The NDBC also uses a man–machine mix of quality checks including graphical procedures which relate spectral wave energy and wind speed (Gilhousen, 1987). The reported wind speed accuracy is ±1.0 m s^{-1} and the reported accuracy of the wind direction is ±10°. A discussion of the data quality in the NDBC buoy winds was performed by Freilich and Dunbar (1999). In addition to the NDBC quality control, we checked the data for outlying wind values, and for errors in the data record such as repeated measurements, and consistent time stamps.

Deleterious effects of missing data at the highest temporal resolutions were diminished by parsing each time series into 30-d segments. Data gaps smaller than 5% of the 30-d records (i.e. not longer than about 1.5 d) were filled using a spline algorithm. Those data segments where the gaps were too large were rejected. Long data sets are required to fully characterize the statistical nature of these oscillations. Even though a local approach (the S-transform) is employed, many realizations of these build up a statistically reliable picture of the phenomena.

Vector wind accuracies can be affected by mooring motion due to ocean tides and currents. Mooring tether designs permit a limited scope for lateral drift in the surface structure. The maximum drift in all directions from the nominal mooring position defines the so-called ‘watch circle’. Typical watch circle diameters are of the order of 500 m. Ocean tidal motion can advect the buoy surface structure across the watch circle in a periodic way that might confound detection of surface wind variability on local inertial time-scales. However, for a diurnal tidal current, a typical watch circle diameter might be transited every 12 h, leading to an erroneous apparent wind velocity of about 0.01 m s^{-1}. This error is not significant with respect to the reported wind speed accuracies noted above. In the event of a passing atmospheric front, the buoy surface structure might be advected across the watch circle diameter, in the direction of propagation of the frontal system, on time-scales of the order of 1 h. While the direction of propagation will lead to consistent underestimates of the wind speed, the amplitude is again below the accuracy resolution of the data.

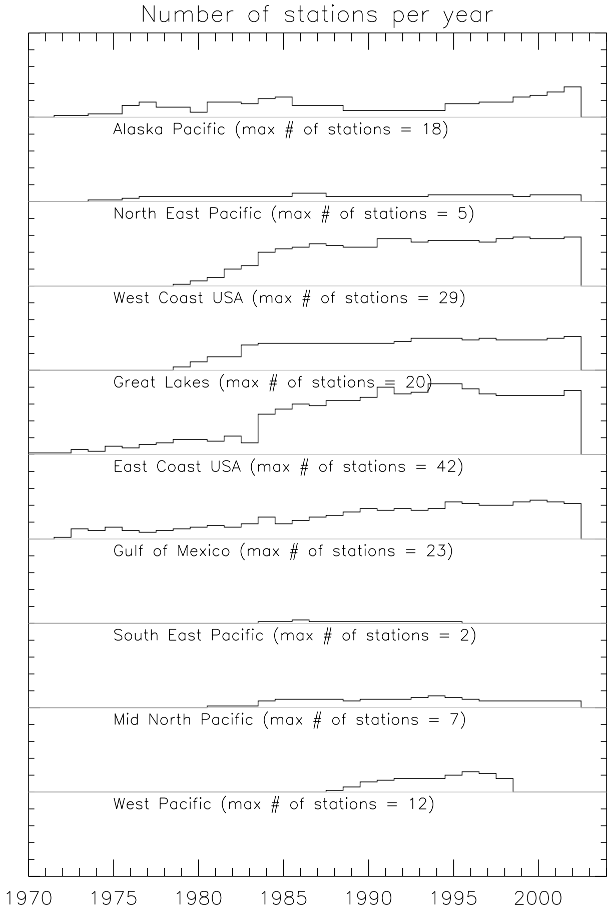

Fig 2. Number of stations reporting data per year for each region (from the NDBC historical STDMET data set). The name of the region is just below the trace, and indicates the maximum number of stations reporting data in any given year for that region. Ordinate tickmarks are at every 10 stations. (See http://seaboard.ndbc.noaa.gov/.)

2.1. Geographic distribution

The non-uniform spatial sampling of the data set must be considered when evaluating the results of the inertial range frequency

Table 1. Description of geographical regions for the moored buoy data set

Region	Latitude Range	Longitude Range
West Pacific	2 to 20	120 to 180
Mid North Pacific	10 to 30	−180 to −140
South East Pacific	−20 to −5	−120 to −60
Gulf of Mexico	20 to 32	−100 to −82
East Coast USA	20 to 55	−82 to −60
Great Lakes	41 to 49	−91 to −75
West Coast USA	32 to 50	−126 to −117
North East Pacific	36 to 52	−138 to −129
Alaska Pacific	50 to 80	−180 to −132

analysis. Many of the moored buoys are in coastal regions and around islands. The land–sea interface may bias the type of signals observed at these sites, such as the atmospheric tidal signals, which may not necessarily be representative of the ocean surface wind field as a whole. In order to establish how important this effect is, the data sets were partitioned into geographic regions as defined in Table 1. As can be seen in Fig. 1, the global coverage is poor, with the data buoys almost entirely in the Northern Hemisphere, significantly clustered off the shore of North America.

3. Analysis of rotating vector time series

Following Hayashi (1979), power spectral analysis can be applied to a two-component vector time series such as the horizontal wind field [$u(t)$, $v(t)$] by constructing a one-dimensional complex valued time series as follows

$$U[t] = u[t] + \mathrm{i}v[t] = A(t)\mathrm{e}^{\mathrm{i}\omega t} \qquad (1)$$

where $u[t]$ is the zonal wind (positive eastward), $v[t]$ is the meridional wind (positive northward), $i = \sqrt{-1}$, ω is the radial frequency of rotation, and $A(t)$ is the amplitude function. The Fourier transform of a complex valued time series requires both the positive and negative frequencies to completely characterize the wind. Such 'rotary spectral' analysis will decompose the wind motions into circular (clockwise and counterclockwise) components.

This representation (eq. 1) is particularly appropriate for inertial motions because of their inherently rotational nature (Orlic et al., 1988). Their rotational frequency is given by the Coriolis parameter, $f = 2\Omega\,\sin(\phi)$, at a latitude ϕ, and planetary rotation rate Ω in rad s^{-1}. The local inertial period ($2\,\pi/f$), therefore, increases monotonically from one-half of a sidereal day (11 h 58 min 2 s) at the pole to the temporal mean ($f = 0$) at the equator. Latitudes $\phi \approx \pm\,30$ are special, because the inertial period is about equal to the 24-h tidal period (Hendershott, 1973; Simpson et al., 2002). The rotation is always anticyclonic. In the Northern (Southern) Hemisphere, ϕ and hence f are positive (negative) and the rotation clockwise (counterclockwise). If spectral frequencies ω from eq. (1) are normalized by f

$$n = \frac{\omega}{-f}, \qquad (2)$$

then $n \simeq 1$ indicates possible inertial resonance with ocean surface currents in both hemispheres because there is wind rotation at the local inertial frequency and in the anticyclonic sense.

4. Power spectral estimation

To search for evidence of inertial motions in the surface winds, high-resolution power spectral density estimations were calculated from the moored buoy data sets. Regularly sampled, 30-d segments of hourly surface wind data were analyzed using the pre-whitened–post-darkened spectral estimation algorithm (Percival and Walden, 1993) with bootstrap confidence intervals (Wikle et al., 1999; Politis et al., 1992).

Figure 3 is the pre-whitened–post-darkened power spectra with bootstrapped confidence intervals (95%) of the monthly vector surface winds from the entire NDBC moored buoy data set. This power spectrum is calculated from over 19 000 monthly time series from 262 data buoy sites. Because of this huge data

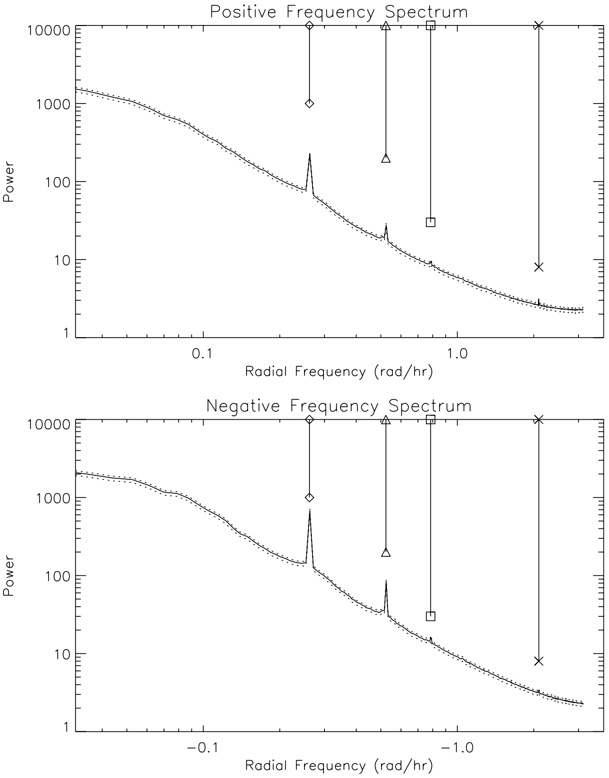

Fig 3. Power spectra as functions of radial frequency for the entire NDBC historical data set of surface winds. The vertical lines denote tidal harmonics (24, 12, 8, and 3 h). The dotted traces indicate the 95% confidence intervals. (a) Positive frequency spectrum and (b) negative frequency spectrum plotted versus ω.

volume, atmospheric tidal signatures and their harmonics are well resolved in significant peaks for both positive and negative frequencies at periods of 24 and 12 h; with small but significant peaks at 8 h, and a peak at 3 h in the positive frequency spectrum. Atmospheric tidal signatures have also been observed in measurements from the Tropical Atmosphere–Ocean moored data buoy array (Deser and Smith, 1998).

Because of the geographical locations of the buoys, the results of the power spectrum (Fig. 3) analysis are not representative of the entire ocean surface, and are heavily biased towards the coast of North America. Positive frequencies represent cyclonic rotation in the Northern Hemisphere, and anticyclonic rotations in the Southern Hemisphere. Land–sea boundary regions could be disproportionately affected by atmospheric tide signals in the surface winds. To examine the importance of these potential offsets, we subdivided the total buoy data set into eight regions to look for land–sea effects in the surface wind power spectra. In each of the power spectra (Fig. 4), tidal signatures (24, 12, and 8 h) can be seen. The higher harmonics are more marginally significant (i.e. the 8-h peak), and the 3-h signal is not significant given the reduced number of data that comprise each regional spectral estimate. At all locations and at all frequencies, the anticyclonic power exceeds the cyclonic power indicating that the winds tend to rotate in an inertial sense; therefore, the Southern Hemisphere data buoys contributing to the spectra in Fig. 3 tend to obscure or reduce this effect.

The tidal signal from near coastal regions is not markedly different from those at more offshore and deep ocean locations, where land–sea effects are negligible. By the nature of the power spectrum, only signals that are coherent over time interfere constructively in the integration (or summation) of the Fourier kernel. Signals, such as inertial winds, that are transient or occur often but out of phase, will be strongly attenuated in the power spectrum. Therefore, the only potentially inertial signals detected by this spectral analysis are the 24-h tidal signals from buoys near 30°. Even though rotation does not dominate these winds, the power at $\omega = -f$ $(n = 1)$ could resonate with ocean surface currents without a compensating response to the power at $\omega = f$ $(n = -1)$. There are no buoys near the poles where f corresponds to a period of 12 h.

5. Resonant inertial range oscillations

In order to estimate the occurrence of possibly strong transient inertial range oscillations, a joint time–frequency representation is employed.

5.1. *Joint time–frequency analysis of the two-component wind*

The S-transform $S(t, \omega)$ is a joint time–frequency representation that produces an image of the spectrum as it changes with

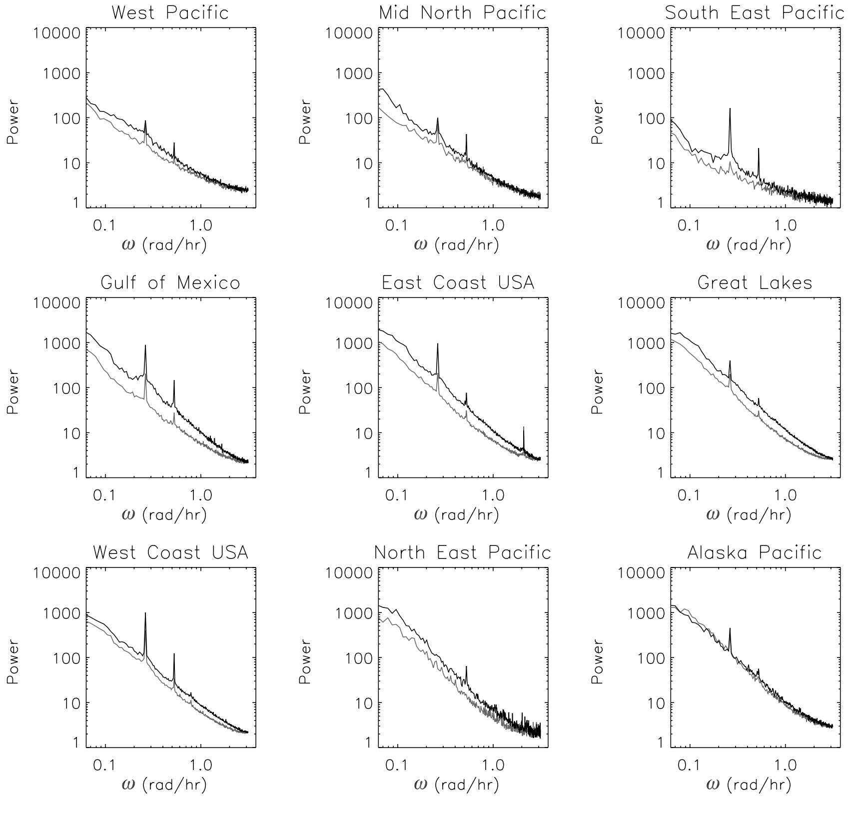

Fig 4. Power spectra determined from each of the nine geographic regions (dark line is the anticyclonic spectra, light line is the cyclonic spectra). Each has strong evidence of the diurnal atmospheric tidal signal, as well as its harmonics. Of the higher harmonics, the 8 h is just barely detectable, and there is no evidence of the 3-h oscillation due to the reduced number of data and lower signal-to-noise ratio.

Table 2. A comparison between different basic two-dimensional motions and the resulting local spectral amplitude

Vector Motion	Effect on local spectra
Circular clockwise	Purely negative frequencies
Circular counterclockwise	Purely positive frequencies
Elliptical clockwise	Negative frequency dominant
Elliptical counterclockwise	Positive frequency dominant
In(De)creasing Spiral	In(De)creasing amplitude
Linear	Positive and negative frequency amplitude equal

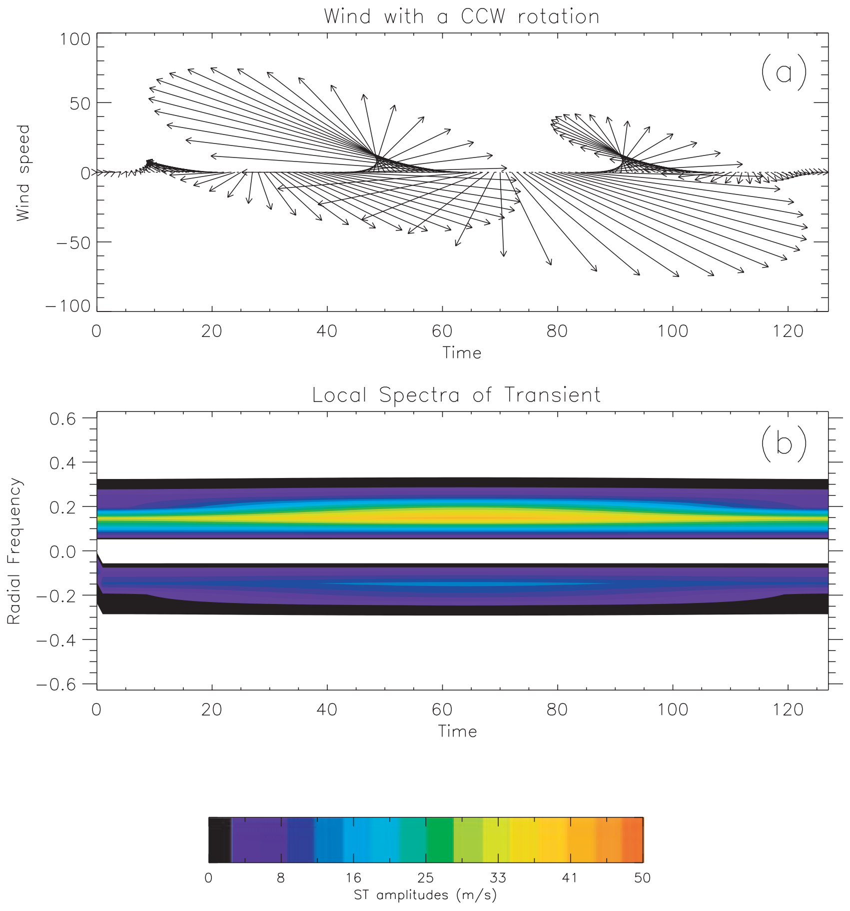

Fig 5. Example of S-transform analysis of a synthetic vector wind time series [u, v]. (a) The time series consists of a spiral rotating counterclockwise that initially increases in amplitude, then in the second half decreases in amplitude. (b) The S-transform amplitudes as a function of time (x-axis) and radial frequency (both negative and positive, y-axis). The changing amplitude can be seen in the shade of the S-transform amplitude. The peak at $\omega = +2\pi 3/128$ is larger (yellow) than the ST amplitude peak at $\omega = -2\pi\, 3/128$ (blue), indicating a counterclockwise motion.

time (Stockwell et al., 1996). As with the Fourier transform, the S-transform can be applied to a two-component vector time series such as the horizontal wind field [$u(t)$, $v(t)$] by constructing a one-dimensional complex valued time series as in eq. (1). The S-transform interpretations for a variety of canonical rotating time series are summarized in Table 2.

By looking at the phase difference between the positive and negative frequencies, it is possible to infer complete information of the generalized elliptical motion, including the sense of rotation, the major and minor axes, and ellipticity.

Inertial range motions can be detected via the S-transform by locating amplitude peaks in the row corresponding to the inertial frequency ($n = 1$). As noted in Table 2, if, in the ratio of the positive frequency to negative frequency amplitudes, the positive frequency is larger, then rotation is counterclockwise (east to north). A synthetic time series illustrating this effect is shown in Fig. 5. The complex time series depicts a counterclockwise rotating surface wind vector, with an amplitude that starts small, grows in time, then decays. The time series was constructed in the form of eq. (1) as follows: $U[t] = 80\cos(2\pi t3/128 + 0.7) + \imath\, 80\sin(2\pi t3/128)$. Here, $t = 0, 1\ldots 127$ and the amplitude is varied by multiplying the time series with a Hanning window. The amplitude of the S-transform of this time series is shown in Fig. 5b. The white background denotes regions of negligible

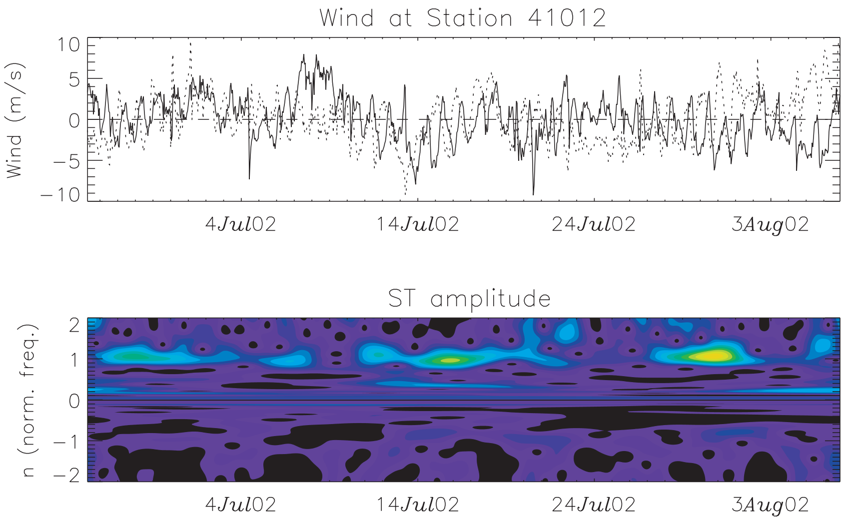

Fig 6. Illustration of inertial range oscillation S-transform analysis of observed winds from station 41012 (30.0N, 80.5W) for summer 2002. (a) Time series wind (zonal, solid line; meridional, dotted line). (b) The S-transform amplitudes showing the time-varying spectrum. Inertial frequencies (positive and negative) are indicated on the radial frequency (y) axis.

energy, and yellow regions correspond to large amplitudes. The peak amplitude occurs at $\omega = 2\,\pi\;3/128$ and $t = 64$. Because this amplitude is larger than its mirror in the negative frequencies ($\omega = -2\pi 3/128$ and $t = 64$), this represents a counterclockwise oscillation. If the negative frequency is larger, then rotation is clockwise (north to east).

Variable winds can excite inertial oscillations in ocean currents, including the sudden onset of a steady wind, and changes in wind direction due to a frontal passage for example. In particular, there can be a very energetic resonant ocean response to winds with a ‘resonant inertial oscillation’ (Large and Crawford, 1995), which we define as a wind rotation at the inertial frequency ($n \approx 1$), with $S(t, n = 1) > S(t, n = -1)$. Subsequent winds usually dampen these inertial currents, but when resonant and in phase they can re-excite pre-existing currents.

Each station in the buoy data set was analyzed using the S-transform technique and normalized frequency (eq. 2). We are looking for amplitudes and frequency of occurrences of inertial oscillations in the surface winds. For example, Fig. 6 shows data from September, 1985 at Moored Data Buoy 41012 (30.0N, 80.5W) from the East Coast USA region. The power spectrum is shown in Fig. 7. For this latitude, the strong tidal signature is the dominant mid-frequency feature and the associated anticyclonic rotation decidedly favors inertial resonance [$S(t, n = 1) \gg S(t, n = -1)$].

The vertical lines indicate the inertial range of frequencies, which contain the tidal signature. Note that the tidal signature is also somewhat transient, in that its amplitude varies over time (Fig. 6). The key feature that differentiates tidal oscillations from inertial range oscillations is that the tidal oscillations always have a consistent phase (for instance, they peak at the same time of the day) even as their amplitude waxes and wanes. The inertial range oscillations do not exhibit this consistent phase pattern.

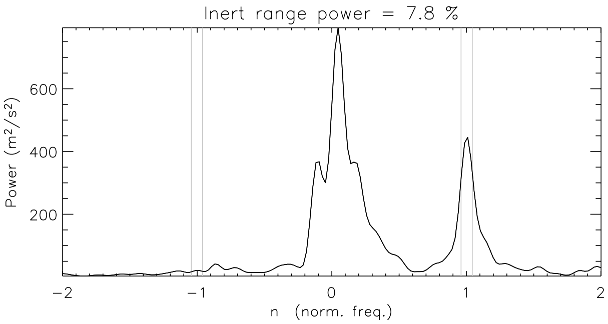

Fig 7. Illustration of inertial range oscillation power spectrum analysis. Tidal and inertial range frequencies coincide at this latitude. Large power spectral amplitudes result from the coherent phase contributions at this frequency.

In Fig. 8, the S-transform analysis of a single station (41002 at 32.27N, 75.42W) is shown. The length of the data record is over 22 yr, from 1979 to 2001. A ‘voice’ of the S-transform is defined as the one-dimensional function of time that gives the local spectrum at one particular frequency. For example, $S(t, n = 1)$ is the voice corresponding to the resonant inertial oscillation for this station (a period of 22.5 h at 32.27N). The voices for both the positive frequency in blue [$S(t, n = -1)$] and the negative frequency in orange [$S(t, n = 1)$] are plotted in Fig. 8a for the entire 22-yr period. There is one very large peak in the orange [$S(t, n = 1)$] voice in September 1985, corresponding to an S-transform amplitude of approximately 5 m s^{-1}. This amplitude is almost an order of magnitude larger than the background amplitude as seen in Fig. 8b.

In addition to this large amplitude peak, there are many peaks in the orange [$S(t, n = 1)$] voice with an amplitude over 2 m s^{-1}. Details of the distribution of resonant inertial oscillation amplitudes are given in Section 5.4. S-transform inertial range voice analyses are shown in Fig. 9 for stations in several geographical regions of Table 1.

In the majority of measurements, as with the tidal motions (Figs. 6 and 7) the negative frequency component dominates the

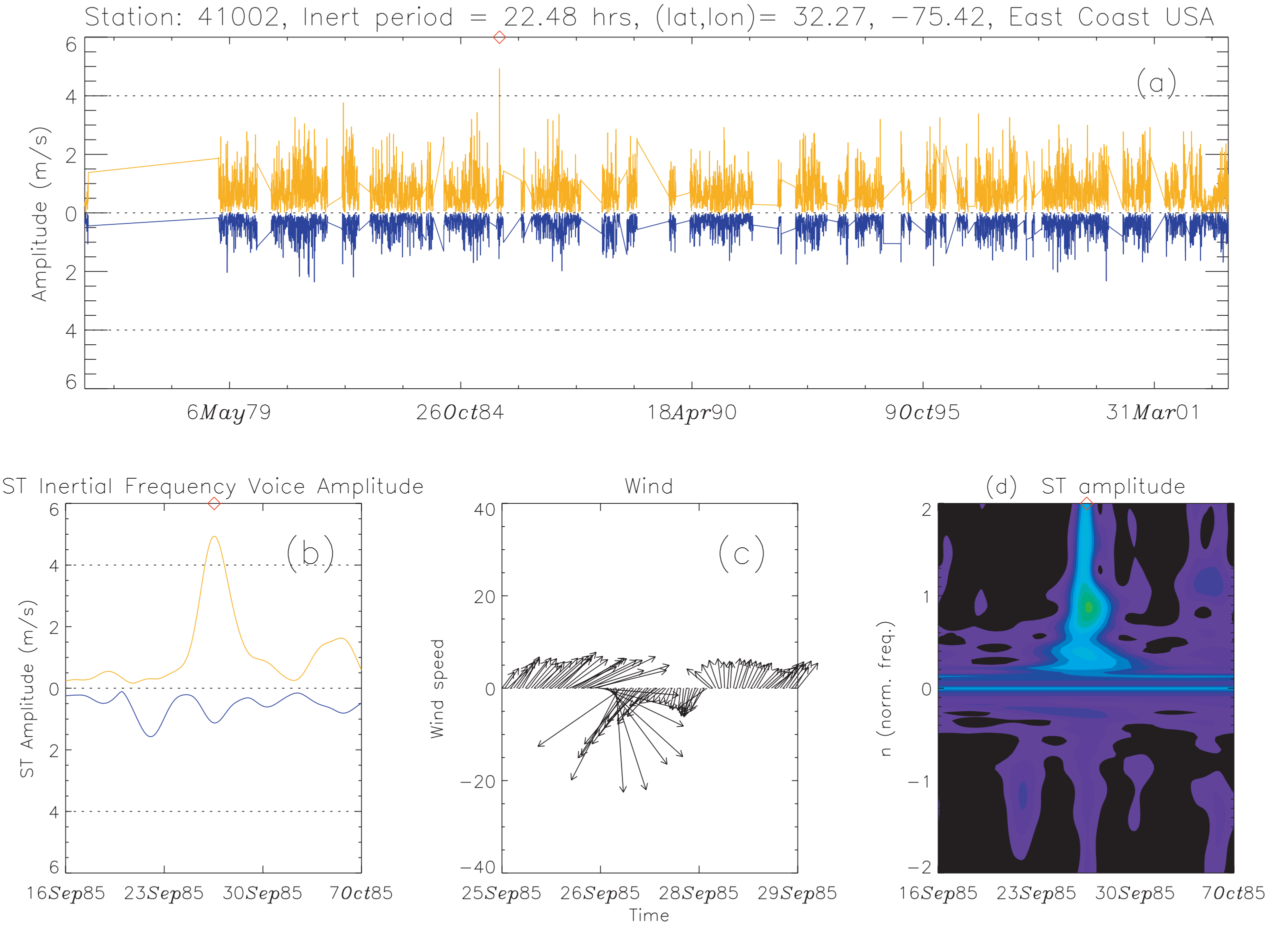

Fig 8. S-transform analysis of inertial oscillations for station 41002 (32.27N, 75.42W). (a) S-transform amplitude of the inertial oscillation frequency (1/22.48 h) voice ($n = -1$ is blue and $n = 1$ is orange) for the entire 22-yr period. (b) Same as in (a), but restricting the time axis to a three-week period. There is a maximum in the S-transform (t, $n = 1$) voice. (c) The time series of the wind over a 4-d period . The clockwise rotation of the wind vector is apparent, as well as the sudden increase in wind amplitude. (d) S-transform over that same three-week time period. The voice shown in (b) is the row corresponding to the $n = 1$ (orange in *b*) and $n = -1$ (blue in *b*).

positive frequency (dark) component [$S(t, n = 1) > S(t, n = -1)$]; corresponding to anticyclonic rotation.

5.2. *Latitude dependence of the resonant inertial oscillations*

In Fig. 10a, the percentage of measurements of inertial oscillations that are resonant is shown as a function of latitude. Almost all stations report the majority of observations as being resonant at the inertial period; in some cases over 80% of the observations are resonant. The region around 30°N has the largest percentage of resonant observations, which suggests a generation mechanism involving atmospheric tides. The distribution of percentages about the peak at 30°N is skewed such that higher percentages occur at latitudes to the north, relative to percentages in latitudes an equal distance to the south. Moreover, the standard deviations indicated in Fig. 10a demonstrate that this skewness is statistically significant. One contributor to this effect might be the non-linear (sinusoidal) variation in inertial period with latitude. Latitudes to the north of 30°N are consistent with inertial periods closer to 24 h than corresponding latitudes to the south, possibly facilitating the tidal generation mechanism suggested above. Another possible contributor to resonant inertial oscillations in latitudes north of 30°N might be a mechanism associated with the passage of atmospheric fronts, i.e. more prevalent in the storm track latitudes than in subtropical latitudes.

In Fig. 10b, the mean inertial frequency voice amplitude for each station as a function of latitude is shown. There is a pronounced peak around 30°N, where the inertial period is 24 h. There is also significant energy in the mean inertial oscillation amplitude at higher latitudes. This indicates that the inertial range oscillation is important at these higher latitudes where the period differs from the diurnal tide. The light gray lines indicate

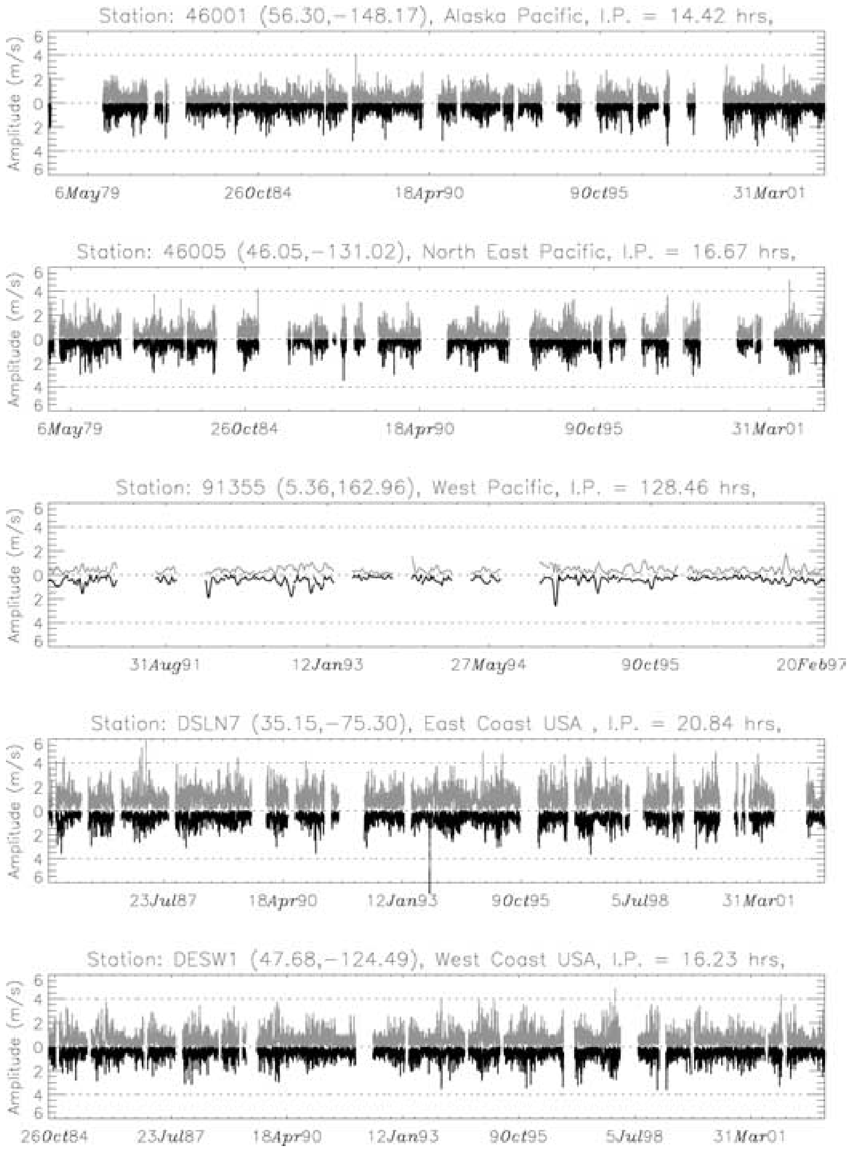

Fig 9. Similar to Fig. 8a (the light trace is $n = 1$, the dark trace is $n = -1$), S-transform voices at the inertial range frequency for selected stations from several regions. The time axis ranges over many years. The amplitude of $S(t, n = 1)$ is greater than $S(t, n = -1)$ almost everywhere.

the standard deviation about the mean. The standard deviation north of 20°N remains fairly constant at ≈ 0.5 m s^{-1}.

Figures 10a and b distinguish latitudinal variations in resonant inertial oscillations that were not apparent in rotary spectra (not shown). The rotary coefficient (Emery and Thomson, 2001) can be written for the Northern Hemisphere in our notation as

$$R = \frac{[S(t, n < 0) - S(t, n > 0)]}{[S(t, n < 0) + S(t, n > 0)]}. \tag{3}$$

When $R = +\,(-)1$, counterclockwise (clockwise) motion is indicated, while $R = 0$ indicates linear motion. In an analysis similar to that shown in Fig. 10a, R peaked at about -0.5 ± 0.1 for latitudes 0° to 60°N, indicating clockwise elliptical motion. There was no appreciable amplitude at $R = 0$ at any latitude in our analysis.

Because inertial frequency increases with increasing latitude, one can think of the x-axis in Fig. 10 as a rescaled frequency axis (as in, for example, Fig. 3). Comparing Fig. 10 with Fig. 3 in this context, note that power decreases with increasing frequency in Fig. 3 where only coherent signals can contribute. In Fig. 10b, amplitude is comparable across all frequencies (i.e. latitudes) demonstrating contributions from incoherent signals that survive in the S-transform analysis. In the power spectrum, the diurnal tidal signal dominates the spectrum (with an amplitude several times larger than the next higher frequencies).

5.3. *Seasonal variations of the inertial range S-transform voice amplitudes*

In order to examine the seasonal variation of the inertial range oscillation amplitudes, a composite year was created for each of

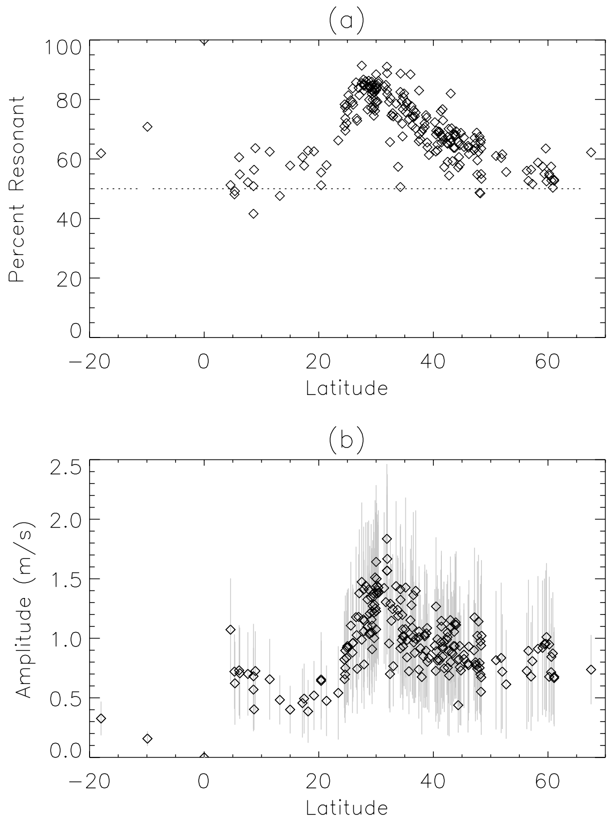

Fig 10. (a) The percentage of the hours of observation in which the oscillation is 'resonant', i.e. $S(t, n = 1) > S(t, n = -1)$. (b) The mean inertial frequency voice amplitude for each station as a function of latitude. There is a pronounced peak around 30°N, where the inertial period is 24 h. There is also large significant energy at higher latitudes. The gray vertical lines indicate the standard deviation.

the geographic regions (Fig. 11). A monthly (30-d) smoother was applied to the data. The negative frequency component amplitude is plotted as the darker line corresponding to an anticyclonic motion in the Northern Hemisphere, i.e. in the sense of resonant inertial oscillations.

Regions in the Pacific show a strong annual cycle of spectral power at $n = 1$. In the North and North-East Pacific, the large fall and winter inertial wind forcing has been attributed to the west to east passage of frontal systems (Large and Crawford, 1995). There is some damping of this cycle along the western coasts of North America, including Alaska. The East Coast of the US, and the Gulf of Mexico have a large inertial ($n = 1$) amplitude throughout the year, suggesting a different generating mechanism. With few exceptions, all regions show the inertial frequency ($n = 1$) dominating over $n = -1$ throughout the year.

5.4. *Distribution of inertial range oscillation amplitudes*

To estimate the relevance of the inertial range oscillations, a statistical histogram analysis was performed. The histogram of Fig. 12 summarizing the inertial oscillation amplitude for every hour for each station in the entire buoy data set is shown, as a percentage of the total number of hours of observations (14 027 937 hourly observations from the over 200 data buoys in operation over the past several decades). Because there are an identical number of hours for both the $n = 1$ and $n = -1$ components, the area under each curve is the same. There is clearly a preponderance of higher amplitude oscillations in the anticyclonic frequency component, consistent with resonant inertial oscillations ($n = 1$).

6. Discussion and conclusion

The spatial sampling provided by the data buoys is sparse, and representative of the seas off North America and equatorial latitudes only. It is heavily weighted to small regions, especially the east and west coasts of the USA, and the Gulf of Mexico. Clearly, better spatial sampling is required to gain a clearer picture of the prevalence of inertial oscillations and their importance to atmosphere-ocean coupling. Previous work (Chin et al., 1998; Milliff et al., 2004) has shown that surface winds from numerical weather prediction products are deficient at the spatial scales of meteorological phenomena implicated in this study (e.g. atmospheric frontal systems). Two broad-swath SeaWinds scatterometers retrieved global surface vector winds for the period May to October 2003. Unfortunately, the 'tandem scatterometer mission' was truncated with the untimely demise of the second scatterometer platform (Midori-II) before an annual cycle could be sampled. Also, the exact nature of the atmosphere–ocean interaction is important to understand. Further ocean modeling work needs to be performed to determine the impact of these transient yet strong inertial frequency oscillations on the underlying ocean motions.

There are significant large amplitude inertial range frequency events in the ocean surface winds as measured by the NDBC moored buoy historical STDMET data set. The intermittent nature and the incoherence over long time periods obscure these events from long-term statistical analysis such as power spectral estimation. Joint time–frequency representations such as the S-transform are appropriate techniques for the detection and study of these types of motions.

Strong surface wind forcing events project on to inertial resonant oscillations, and provide the possibility of a strong coupling mechanism for atmosphere–ocean transfer.

Inertial range frequency is a function of latitude. In the region around 30°N/S, the inertial frequency is equal to the atmospheric diurnal tidal frequency (≈24-h periods). The diurnal atmospheric tide in the surface wind may provide a major conduit for atmosphere–ocean transfer in this region. At other latitudes, inertial oscillations from sources such as frontal passage (Pollard, 1980) may be a major mechanism for atmosphere–ocean transfer. The NDBC buoy record shows that surface wind rotation direction in near inertial frequency bands favors resonant

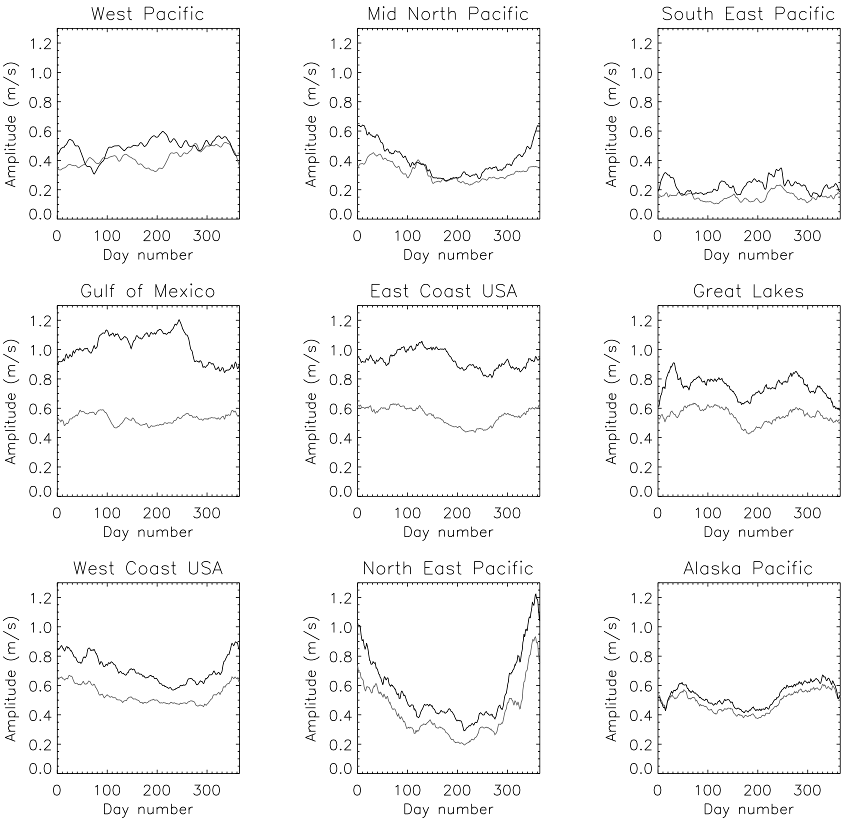

Fig 11. A composite year of the inertial frequency amplitudes for each geographical region. The dark line indicates anticyclonic oscillations ($n = 1$). The time axis is day number.

inertial oscillations (i.e. $n = 1 > n = -1$) at all latitudes, and in every season of the year.

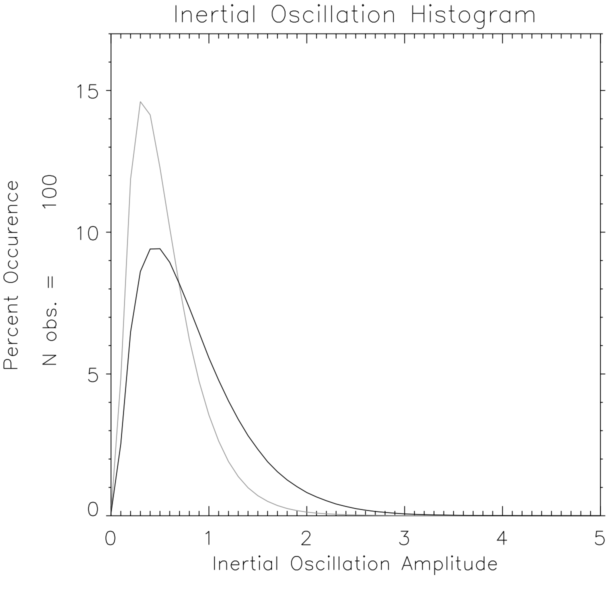

Fig 12. Histogram of the inertial range S-transform voice (i.e. the amplitude of the inertial range oscillation) for the entire moored buoy data set. The dark line indicates resonant oscillations ($n = 1$), which are a possible avenue for resonant atmosphere–ocean coupling.

7. Acknowledgments

This work has been partially supported by National Oceanic and Atmospheric Administration (NOAA) grant no. NA06GP0428 and by the National Science Foundation through its support of National Center for Atmospheric Research (NCAR). We are grateful to the NDBC for making these data available at http://seaboard.ndbc.noaa.gov/.

8. Appendix A: The S-Transform

The continuous S-transform of a function $h(t)$ is defined as (Stockwell et al., 1996; Stockwell and Lowe 2001a,b)

$$S(\tau, \omega) = \frac{|\,\omega\,|}{2\pi\sqrt{2\pi}} \int_{-\infty}^{\infty} h(t) \mathrm{e}^{-[(t-\tau)^2\omega^2]/8\pi^2} \mathrm{e}^{-\mathrm{i}\omega t} \mathrm{d}t. \qquad \text{(A1)}$$

Note that the ‘localizing in time’ Gaussian window $\exp(-[(t - \tau)^2\, \omega^2]/8\, \pi^2)$ translates in time $(t - \tau)$, while the Fourier kernel $\exp(-\,\mathrm{i}\omega\, t)$ does not. This distinguishes the S-transform from a continuous wavelet transform and gives the S-transform absolutely referenced phase information.

In the discrete case, the S-transform of a time series $h[kT]$ with a Fourier transform $H[p/NT]$ is defined as

$$S\left[jT, \frac{p}{NT}\right] = \textstyle\sum_{q=0}^{N-1} H\left[\frac{q+p}{NT}\right] \mathrm{e}^{-(2\pi^2 q^2/p^2)} \mathrm{e}^{(\mathrm{i}2\pi qj/N)}, \quad p \neq 0, \tag{A2}$$

and for the $p = 0$ voice it is equal to the constant defined as

$$S[jT, 0] = \frac{1}{N} \sum_{q=0}^{N-1} h\left(\frac{q}{NT}\right), \tag{A3}$$

where j, q, and $p = 0, 1, \ldots, N - 1$. Equation (6) puts the constant average of the time series into the zero frequency voice, thus assuring the inverse is exact for the general time series.

Properties of the S-transform

Because of the absolutely referenced phase information in the S-transform, many advantageous characteristics arise as follows.

(1) Inverse of the S-transform is via the inverse Fourier transform (Stockwell et al., 1996):

$$h(t) = \frac{1}{2\pi} \int_{-\infty}^{\infty} \left\{ \int_{-\infty}^{\infty} S(\tau, \omega)\, \mathrm{d}\tau \right\} \mathrm{e}^{\mathrm{i}\omega t}\, \mathrm{d}\omega. \tag{A4}$$

(2) The progressive resolution of the time–frequency domain, where long periods have good frequency resolution and short-period signals have good time resolution, gives a fundamentally more sound time–frequency representation (Daubechies, 1990) than a fixed resolution representation.

(3) The S-transform defines a generalized instantaneous frequency (GIF). One can write the S-transform as a complex function

$$S(\tau, \omega_\mathrm{o}) = A(\tau, \omega_\mathrm{o}) \mathrm{e}^{\mathrm{i}\Phi(\tau, \omega_\mathrm{o})}, \tag{A5}$$

then the generalized instantaneous frequency is defined as (Stockwell et al., 1996)

$$IF(\tau, \omega_\mathrm{o}) = \frac{1}{2\pi} \frac{\partial}{\partial \tau} \{\tau \omega_\mathrm{o} + \Phi(\tau, \omega_\mathrm{o})\}. \tag{A6}$$

(4) The S-transform is linear, and thus the effect of additive noise can be easily modeled.

References

Anderson, I., Huyer, A. and Smith, R. 1983. Near-inertial motions off the Oregon coast. *J. Geophys. Res. – Oceans and Atmospheres* **88**(C10), 5960–5972.

Burt, W., Cummings, T. and Paulson, C. 1974. Mesoscale wind field over ocean. *J. Geophys. Res.* **79**(36), 5625–5632.

Chin, T., Milliff, R. and Large, W. 1998. Basin-scale high-wavenumber sea surface wind fields from multiresolution analysis of scatterometer data. *J. Atmos. Ocean. Technol.* **15**, 741–763.

Crawford, G. and Large, W. 1996. A numerical investigation of resonant inertial response of the ocean to wind events. *J. Phys. Oceanogr.* **26**, 873–891.

D'Asaro, E. 1995. Upper ocean inertial currents forced by a strong storm. Part II: modelling. *J. Phys. Oceanogr.* **25**, 2937–2952.

Daubechies, I. 1990. The wavelet transform, time–frequency localization and signal analysis. *IEEE Trans. Inf. Theory* **36**(5), 961–1005.

Deser, C. and Smith, C. 1998. Diurnal and semidiurnal variations of the surface wind field over the tropical Pacific Ocean. *J. Climate* **11**, 1730–1748.

Emery, W. and Thomson, R. 2001. *Data Analysis Methods in Physical Oceanography*. Elsevier, Amsterdam.

Firing, E., Lien, R. and Muller, P. 1997. Observations of strong inertial oscillations after the passage of tropical cyclone Ofa. *J. Geophys. Res. – Oceans* **102**(C2), 3317–3322.

Freilich, M. and Dunbar, R. 1999. The accuracy of NSCAT-1 vector winds: Comparisons with the National Data Buoy Center buoys. *J. Geophys. Res.* **104**(C5), 11 231–11 246.

Fu, L. 1981. Observations and models of inertial waves in the deep ocean. *Rev. Geophys.* **19**(1), 141–170.

Gilhousen, D. 1987. A field evaluation of NDBC moored buoy winds. *J. Atmos. Oceanic Technol.* **4**, 94–104.

Halle, C. and Pinkel, R. 2003. Internal wave variability in the Beaufort Sea during the winter of 1993/1994. *J. Geophys. Res. – Oceans* **108**(C7), 3210.

Hayashi, Y. 1979. Space–time spectral analysis of rotary vector series. *J. Atmos. Sci.* **36**(5), 757–766.

Hendershott, M. 1973. Inertial oscillations of tidal period. *Prog. Oceanography* **6**, 1–27.

Kudryavtsev, V. 1994. The coupling of wind and internal waves – modulation and friction mechanisms. *J. Fluid Mech.* **278**, 33–62.

Large, W. and Crawford, G. 1995. Observations and simulations of upper ocean response to wind events during the Ocean Storms experiment. *J. Phys. Oceanogr* **25**, 2832–2852.

Levine, M. and Zervakis, V. 1995. Near-inertial wave-propagation into the pycnocline during ocean storms – observations and model comparison. *J. Phys. Oceanography* **25**(11), 2890–2908.

Milliff, R., Morzel, J., Chelton, D. and Freilich, M. 2004. Wind stress curl and wind stress divergence biases from rain effects on QSCAT surface wind retrievals. *J. Atmos. Ocean. Technol.* **21**(8), 1216–1231.

Mori, Y. 1990. Evidence of inertial oscillations of the surface wind at Marcus Island. *J. Geophys. Res. – Atmospheres* **95**(D8), 11777–11783.

Orlic, M., Penzar, B. and Penzar, I. 1988. Adriatic Sea and land breezes – clockwise versus anticlockwise rotation. *J. Appl. Meteorol.* **27**(5), 675–679.

Percival, D. and Walden, A. 1993. Spectral Analysis for Physical Applications: Multitaper and Conventional Univariate Techniques. Cambridge University Press, Cambridge.

Pereira, C. and Mascarenhas, A. 1994. Numerical simulation of a response of an oceanic front to an atmospheric frontal passage. *J. Geophys. Res. – Oceans* **99**(C8), 16 081–16 094.

Politis, D. N., Romano, J. P., and Lai, T. 1992. Bootstrap confidence bands for spectra and cross-spectra. *IEEE Trans. Signal Process.* **40**, 1206–1215.

Pollard, R. 1980. Properties of near-surface inertial oscillations. *J. Phys. Oceanography* **10**(3), 385–398.

Pollard, R. and Millard, R. 1970. Comparison between observed and simulated wind-generated inertial oscillations. *Deep-Sea Res.* **17**, 153–175.

Pollard, R., Rhines, P. and Thompson, R. 1973. The deepening of the wind-mixed layer. *Geophys. Fluid Dyn.* **3**, 381–404.

Poulain, P. 1990. Near-inertial and diurnal motions in the trajectories of mixed layer drifters. *J. Marine Res.* **48**(4), 793–823.

Qi, H., Deszoeke, R., Paulson, C. and Eriksen, C. 1995. The structure of near-inertial waves during ocean storms. *J. Phys. Oceanography* **25**(11), 2853–2871.

Simpson, J. H., Hyder, P. and Rippeth, T. 2002. Forced oscillations near the critical latitude for diurnal-inertial resonance. *J. Phys. Oceanography* **32**(1), 177–187.

Stockwell, R., Mansinha, L. and Lowe, R. 1996. Localization of the complex spectrum: the S transform. *IEEE Trans. Signal Process.* **44**(4), 998–1001.

Stockwell, R. and Lowe, R. 2001a. Airglow imaging of gravity waves 1. Results fom a small network of OH nightglow scanning imagers. *J. Geophys. Res.* **106**(D15), 17 185–17 203.

Stockwell, R. and Lowe, R. 2001b. Airglow imaging of gravity waves 2. Critical Layer Filtering. *J. Geophys. Res.* **106**(D15), 17 205–17 220.

Webster, F. 1968. Observations of inertial period motions in the deep sea. *Rev. Geophys. Space Phys.* **6**, 473–490.

Wikle, C., Milliff, R. and Large, W. 1999. Surface wind variability on spatial scales from 1 to 1000 km observed during TOGA COARE. *J. Atmos. Sci.* **56**, 2222–2231.